

Designing hierarchical eutectic high-entropy alloys via partial similar substitution in the Ni-Fe-Ti-Hf-Nb alloys

Huan Li^{a,b,c}, Yongkang Zhou^{a,b,c}, Lili Yu^d, Qi Chen^{a,b,c}, Weizheng Liu^b, Shuai Zeng^{a,b,c}, Huiming Zhang^{a,b,c}, Yuhui Zhu^{a,b,c}, Hongwei Zhang^{a,c}, Haifeng Zhang^{a,c}, Zhengwang Zhu^{a,c,*}

^a Shi-changxu Innovation Center for Advanced Materials, Institute of Metal Research, Chinese Academy of Sciences, Shenyang, 110016, China

^b School of Materials Science and Engineering, University of Science and Technology of China, Hefei, 230026, China

^c CAS Key Laboratory of Nuclear Materials and Safety Assessment, Institute of Metal Research, Chinese Academy of Sciences, Shenyang, 110016, China

^d Qingdao Qingte Zhongli Automobile Axle Co., Ltd., Qingdao, 266000, China



ARTICLE INFO

Keywords:

Alloy design
Eutectic high entropy alloys
Hierarchical structure
Mechanical properties

ABSTRACT

Hierarchical eutectic high entropy alloys show distinguished mobility and castability, the fine lamella structure, and the excellent compression property, but their development still faces challenges. Here, the partial similar substitution method is to design hierarchical eutectic high-entropy alloys. This concept successfully developed a hierarchical eutectic $\text{Ni}_3\text{FeTi}_3\text{HfNb}_2$ high-entropy alloy composed of B2 intermetallic compounds and disordered body-centered cubic (BCC) phases. It displays an outstanding compression property, with the yield strength (σ_y) as high as 1407 MPa, the large fracture strain of 22.1% and the large elastic strain of 3.0%. The combination of high strength and good ductility exhibits a promising application in industry. Moreover, the anisotropy and the relationships among microstructure evolution, mechanical property and Nb concentration are systematically discussed.

1. Introduction

High entropy alloys (HEAs) consisting of multi-principal elements were firstly proposed by Yeh et al. [1] to break through the traditional alloy strategy based on the one or two principal elements, which has already made a significant impact on designing novel materials including alloys and ceramics etc. Worldwide. So far, many HEAs with extraordinary properties have been designed and developed. For instance, Lei et al. designed $(\text{TiZrNbHf})_{98}\text{O}_2$ high entropy alloy, displaying unprecedented tensile properties with an ultimate tensile strength over 1300 MPa and an extended rate exceeding 32% [2]. The NiCoFeCrMn HEA exhibits an enhanced radiation tolerance by controlling defect mobility and migration pathways [3]. However, due to multi-principal elements, the composition complexity leads to HEAs showing poor castability, liquidity, and significant inhomogeneity [4–8]. To overcome the abovementioned issue, Lu et al. proposed as-cast eutectic high entropy alloys (EHEAs) in 2014 [9]. Extensive works have shown that such as-cast EHEAs possess the good castability as well as the good balance between strength and ductility, showing the great

application potential as engineering structural materials.

However, in spite of above outstanding properties, the most as-cast EHEAs show the low yield strength. For instance, the as-cast $\text{Fe}_{20}\text{Co}_{20}\text{Ni}_{41}\text{Al}_{19}$ EHEA has a low yield strength of 577 MPa at the room temperature [10], and the as-cast $\text{AlCoCrFeNi}_{2.1}$ alloy has a proof stress of only 75 MPa at the room temperature [9]. Therefore, to overcome this problem, the hierarchical EHEAs were developed to improve the yield strength using several methods, i.e., cold-rolling and annealing, directional solidification [11,12]. For instance, a dual-phase hierarchical eutectic structure of a cold-rolled and annealed $\text{AlCoCrFeNi}_{2.1}$ alloy exhibits the high tensile yield strength of about 1.4 GPa [11]. Shi et al. [12] prepared the herringbone high-entropy alloy using a directionally solidified technique, which showed the yield strength of ~670 MPa, the high tensile ultimate strength of ~1060 MPa and the tensile elongation of ~50% due to hierarchical crack buffering.

Although hierarchical eutectic high entropy alloys (EHEAs) are promising due to their various excellent properties, their development still faces challenges. Therefore, in the current work, a partial similar substitution was employed to design new hierarchical EHEAs, as shown

* Corresponding author. Shi-changxu Innovation Center for Advanced Materials, Institute of Metal Research, Chinese Academy of Sciences, Shenyang, 110016 China.

E-mail address: zwzhu@imr.ac.cn (Z. Zhu).

in Fig. 1. Firstly, one known eutectic alloy was selected, which consisted of the disorder solid solution and the ordered intermetallic. Secondly, two or more atoms of the similar elements as the nominal composition of known eutectic alloy, were added to the crystalline lattice to partially substitute the original ones, leading to the lattice distortion effect and the formation of EHEA. In this process, the mixing enthalpy (ΔH_{mix}) values, based on Miedema's model [13], of the original atom and the newly added atom should be closed to 0 kJ/mol, to inhibit the formation of new phases and maintain the eutectic structure composed of the same phases. Finally, in order to obtain hierarchical eutectic structure, the eutectic high entropy alloy should be prepared by the directional solidification technique. The reason is that the solid-liquid interface temperature gradient, created by the directional solidification technique, was helpful to form the coarse dual-phase non-lamellar zone and the fine dual-phase lamellar zone, which forms the hierarchical eutectic structure [12].

In order to prove the feasibility of the above method, we followed this method to prepare the realistic hierarchical eutectic high entropy alloy. Firstly, the $\text{Ni}_{41}\text{Ti}_{39}\text{Nb}_{20}$ composition was chose to be our known eutectic alloy [14]. Secondly, we selected the Fe and Hf atoms to be newly added atoms, because the mixing enthalpy (ΔH_{mix}) values of Fe and Ni atoms, Hf and Ti atoms are respectively -2 kJ/mol and 0 kJ/mol [13], which followed the second rule in partial similar substitution method. Then, we substituted the 11 at.% Fe element for the 11 at.% Ni element, and substituted the 9 at.% Hf for the 9 at.% Ti in the B2 lattice, achieving the $\text{Ni}_3\text{FeTi}_3\text{HfNb}_2$ eutectic high entropy alloy. Finally, to obtain the hierarchical structure, we used the directionally solidified technique to prepare the $\text{Ni}_3\text{FeTi}_3\text{HfNb}_2$ hierarchical eutectic high entropy alloy, and $\text{Ni}_3\text{FeTi}_3\text{HfNb}_{1.5}$ and $\text{Ni}_3\text{FeTi}_3\text{HfNb}_{2.5}$ were also prepared as contrast samples to discuss the effect of Nb concentration on mechanical properties and structures (denoted as Nb1.5, Nb2 and Nb2.5, respectively, in the following, in the atomic percentage).

2. Experimental method

The studied alloys with non-equatomic compositions of $\text{Ni}_3\text{FeTi}_3\text{HfNb}_{1.5}$, $\text{Ni}_3\text{FeTi}_3\text{HfNb}_2$, and $\text{Ni}_3\text{FeTi}_3\text{HfNb}_{2.5}$ alloys were prepared from high pure elements (Ti, Ni, Hf: 99.9 wt%); Fe, Nb: 99.8–99.9 wt%). The raw elements were alloyed in a vacuum, non-consumable arc melting furnace of copper crucibles in a Ti-gettered high-purity argon atmosphere. To obtain the chemical homogeneity, the intermediate alloys, including Ti, Ni and Nb alloys, were melted five times and then, after adding in Fe and Hf, were melted five times again. The rod-like alloy samples with 8 mm in diameter and 150 mm in length were prepared by Edmund-Buhler AM/0.5 high vacuum arc-melting furnace. The directional solidification experiment was carried out by a FZ-T-12000-X-VP-S type optical floating zone furnace. Two rod-like samples were used in this process. The first one was hung by an iron wire on the other one, and the distance between them was 0.5 mm. To start the experiment, the

top one turned with 15 rpm. Light focused on the tail of the top alloy and caused the alloy to melt and join to the bottom alloy, creating a liquid zone in the middle. Then, the focus of light moved upwards at 180 mm/h, so the growth rate in this work was 180 mm/h.

The phase constitution of the alloy was characterized by the X-ray diffractometer (XRD, Rigaku D/max-2500PC) using a Cu target, at a scanning rate of $3^\circ/\text{min}$ and the 20 scanning ranges of 15° – 90° . The microstructure and chemical composition were characterized with scanning electron microscopes (SEM; Tescan MIRA3) and transmission electron microscope (TEM; FEI Talos F200X G2) at 200 kV. The SEM samples were treated by the mechanical polishing, and then chemical etched for tens of seconds by using mixed solution of $\text{HCl}:\text{HNO}_3:\text{H}_2\text{O} = 3:1:4$. The TEM samples were manually grounded by sand-paper until $40 \mu\text{m}$ and then electropolished (electrolyte: 90% methyl alcohol + 10% perchloric acid). The melting and solidification events of all the present alloys were measured with a differential scanning calorimeter (DSC; Netzsch DSC404F) at a heating/cooling rate of 10 K/min. The gauge length, width, thickness of Vickers hardness specimens were designed as 10 mm, 10 mm, 1 mm, respectively. These specimens were grounded by different sandpapers and then were treated by mechanical polishing. The Vickers hardness tests were conducted by the Tukon 1102 under the load of 10 N and the load retention time of 10 s. Each Vickers hardness test was repeated five times to ensure the precision and repeatability. Cylindroid compression specimens with a diameter of 3 mm and a length of 4.5 mm were machined and polished. Room-temperature compression tests were carried out using the Instron 5582 testing machine at a constant strain rate of $1 \times 10^{-3} \text{ s}^{-1}$, and the strain data was monitored using a contact extensometer (Instron 2620-601). To gain the reproducible compression data, at least five specimens were performed for each condition.

3. Results

3.1. Microstructure and phase constitution

Fig. 2 shows the XRD curves of Nb1.5, Nb2 and Nb2.5. It can be seen that all the samples are composed of B2-BCC dual-phase, which is consistent with the results reported in the $\text{Ni}_{41}\text{Ti}_{39}\text{Nb}_{20}$ alloy [14]. It proved that after the partial similar substitution, there is no phase transformation to change the composition of phases. As the content of Nb increases, the intensity of the (110) peak in corresponding the BCC phase increases and eventually surpasses that of the (110) peak corresponding to the B2 phase. It is worth noting that according to the locations of the (110) peaks corresponding to the B2 and BCC phases, a low lattice misfit of $\sim 7.13\%$ is calculated between B2 and BCC phases for Nb2 alloy, which is lower than the lattice mismatch of $\sim 9.23\%$ for $\text{Ni}_{41}\text{Ti}_{39}\text{Nb}_{20}$ [14]. It makes it easier for this B2-BCC dual-phase to become a coherent structure [15].

The cross-section microstructures of Nb1.5, Nb2, and Nb2.5 are

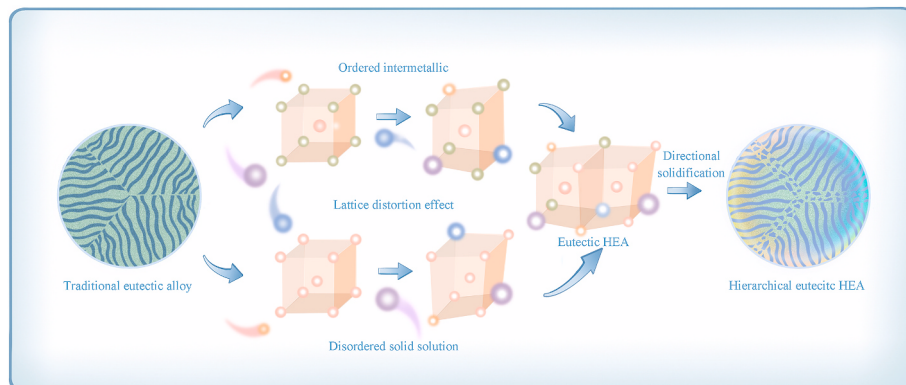


Fig. 1. The schematic of the partial similar substitution method to design the new hierarchical eutectic high-entropy alloy.

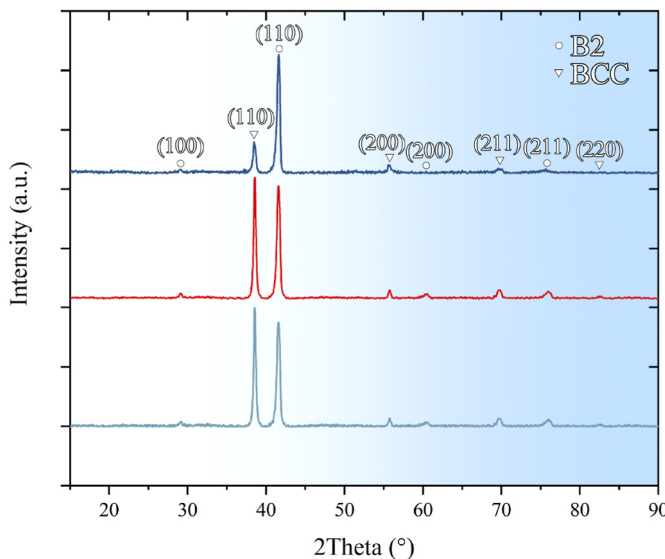


Fig. 2. X-ray diffraction (XRD) curves of the Nb1.5, Nb2 and Nb2.5.

displayed in Fig. 3(a-f). The chemical compositions of all phases are listed in Table 1. It can ensure that the Nb element enriches in BCC phases, while Ni, Fe, Ti and Hf enrich in B2 phases. It is found out that as the Nb content increases in the alloys, the Nb content in the BCC phases increases while the content of Nb in the B2 phases rarely changes. Fig. 3 (a-f) shows the dependence of microstructural evolution with varying Nb content in the alloys. The transformation from hypoeutectic microstructure in the Nb1.5 to eutectic one in the Nb2 to hypereutectic one in the Nb2.5 is apparently illustrated. The primary B2 and BCC phases with a large size were precipitated in the Nb1.5 and Nb2.5 alloys, respectively. Additionally, based on five SEM images per composition, the volume fractions of the BCC phase in the Nb1.5, Nb2, and Nb2.5 alloys are estimated to be $21.8 \pm 1.1\%$, $25.4 \pm 1.7\%$, and $28.5 \pm 1.3\%$, respectively.

The most important thing is that the microstructure of Nb2 consists of the coarse dual-phase non-lamellar zone (CNZ) and the fine dual-phase lamellar zone (FLZ) (Fig. 3(b) and (e)). The FLZ consists of BCC and B2 lamellae, and the average thicknesses of BCC and B2 lamellae in the FLZ are about ~ 200 nm and ~ 700 nm, respectively. However, In the

Table 1

The EDS-determined compositions and corresponding standard deviations of the BCC and the B2 phases in the Nb1.5, Nb2 and Nb2.5.

Alloys	Phases	Ti (%)	Ni (%)	Fe (%)	Hf (%)	Nb (%)
Nb1.5	B2	32.6 ± 0.3	37.4 ± 0.3	11.9 ± 0.1	12.4 ± 0.2	5.7 ± 0.1
	BCC	28.7 ± 0.2	2.2 ± 0.1	1.8 ± 0.1	3.1 ± 0.1	64.2 ± 0.6
Nb2	B2	33.3 ± 0.3	36.4 ± 0.3	12.2 ± 0.1	12.4 ± 0.1	5.7 ± 0.1
	BCC	12.5 ± 0.2	2.3 ± 0.1	1.8 ± 0.1	1.5 ± 0.1	81.9 ± 0.7
Nb2.5	B2	32.2 ± 0.3	37.9 ± 0.2	11.7 ± 0.1	12.1 ± 0.1	6.1 ± 0.1
	BCC	11.4 ± 0.1	2.6 ± 0.1	2.0 ± 0.1	1.4 ± 0.1	82.6 ± 0.6

CNZ, there are large spherical phases and thick lamellae of BCC and B2. The diameter of large spherical BCC phases is ~ 4.24 μm , and the thickness of BCC lamellae is 1.94 μm . In low-magnification SEM image of Nb2 (Fig. 3(b)), the volume fractions of CNZ and FLZ are estimated to be $47.1 \pm 1.9\%$ and $52.9 \pm 2.2\%$, respectively, so the CNZ and FLZ roughly occupied the same volume in Nb2. It is easily to find out that the FLZ were surrounded by the CNZ, where the diameter of FLZ is about 150 μm , and the width of CNZ is about 30 μm . Additionally, the BCC phases with a diameter of ~ 4 μm in CNZ are coarser than BCC phases in FLZ. Such the morphology is consistent with the developed hierarchical microstructure pointed out by Bhattacharjee et al. [16] containing the coarse dual-phase non-lamellar zones and the fine dual-phase lamellar ones.

To further confirm whether the present compositions are fully eutectic or non-eutectic, the melting and solidification peaks were measured by the DSC device. Fig. 4(a-c) presents the DSC curves of the Nb1.5, Nb2 and Nb2.5 alloys, respectively. It can be seen that only one sharp exothermic/endothermic peak is shown in the heating and cooling processes in the Nb2 alloy's DSC curve (Fig. 4 (b)). Its melting interval of 41 $^{\circ}\text{C}$ and solidification interval of 53 $^{\circ}\text{C}$ were pretty narrow, as shown in Fig. 4(b), indicating that the Nb2 alloy is probably eutectic [17]. However, two exothermic/endothermic peaks were shown for Nb1.5 and Nb2.5, as shown in Fig. 4(a) and (c), indicating that Nb1.5 and Nb2.5 are not eutectic. In the DSC curve of Nb1.5, the eutectic structure and large primarily-precipitated B2 phases caused high and low exothermic/endothermic peaks, respectively. In the DSC curve of Nb2.5, the

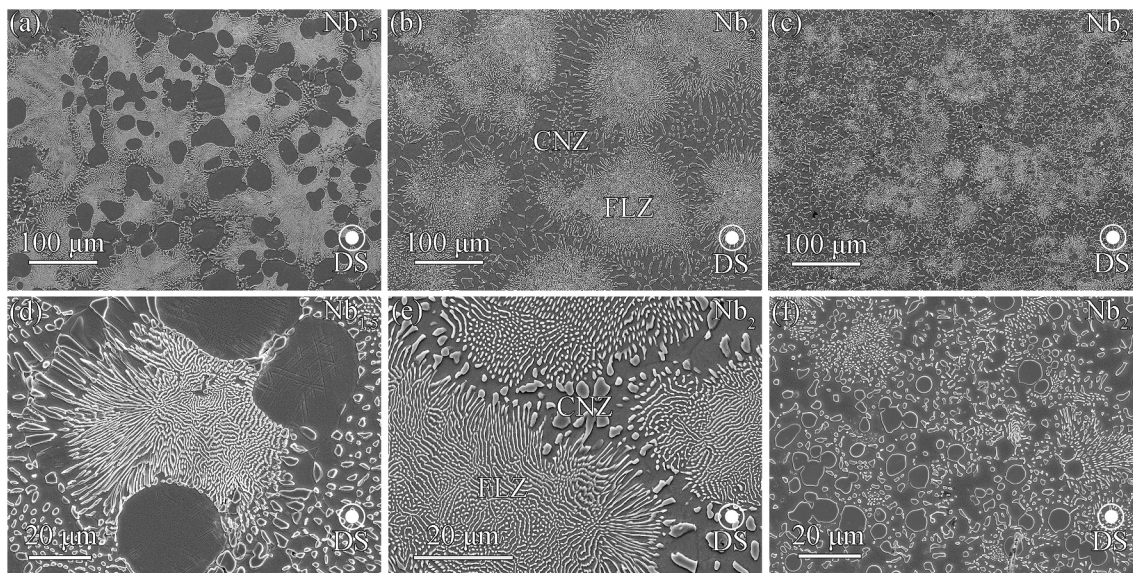


Fig. 3. The scanning electron microscope (SEM) cross-section images of (a) and (d) Nb1.5, (b) and (e) Nb2, (c) and (f) Nb2.5.

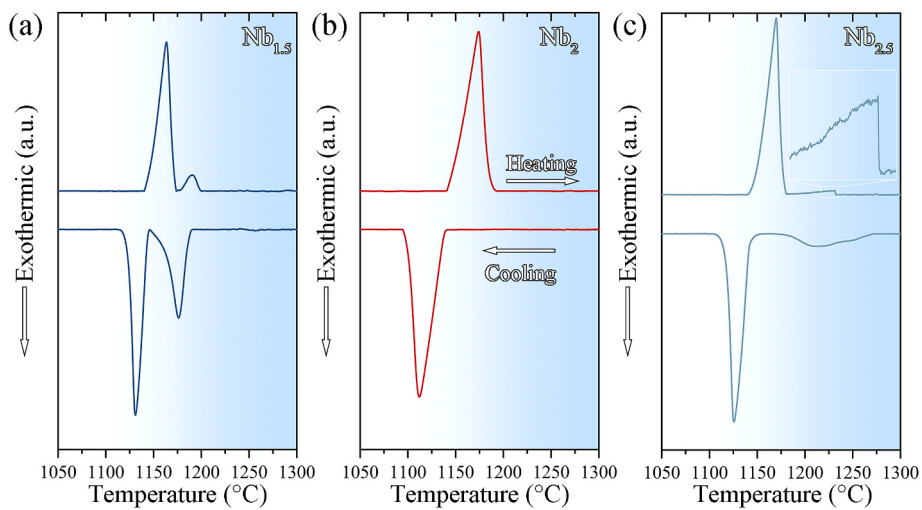


Fig. 4. The differential scanning calorimetry (DSC) curves of the (a) Nb1.5, (b) Nb2 and (c) Nb2.5.

eutectic structure and large primarily-precipitated BCC phases caused high and low exothermic/endothermic peaks, respectively.

Fig. 5 exhibits a typical scanning transmission electron microscopy high-angle annular dark-field (STEM-HAADF) image showing the more detailed microstructure of BCC/B2 lamellae and no other precipitated phases forming. It shows that the average lamellar thicknesses of BCC and B2 are about ~200 nm and ~700 nm, respectively. In STEM-HADDIF imaging conditions, contrast arises from the collection of incoherently scattered high-angle electrons and, therefore, from variations in local atomic number between phases [18]. The STEM energy dispersive spectroscopy (STEM-EDS) mappings in Fig. 5 clearly show the partitioning of Ni, Fe, Ti and Hf to the B2 phase and Nb to the BCC phase, consistent with Table 1.

Fig. 6(a) shows the TEM bright-field parallel to [011] zone of the BCC/B2 phases with the SAED image. The SAED image reveals that the orientation relationship (OR) between the two phases is $<110>_{\text{BCC}}//<110>_{\text{B2}}$, $\{110\}_{\text{BCC}}//\{110\}_{\text{B2}}$. Fig. 6(b) shows a representative high-resolution TEM image. The SAED image proves that the boundary between the BCC/B2 phases is coherent, which is consistent with XRD curves (Fig. 2).

3.2. Mechanical properties

Fig. 7 shows the scanning electron microscope (SEM) images of the representative Vickers hardness points of Nb1.5, Nb2 and Nb2.5, and the lengths of diagonal X and Y, depths and Vickers hardness values of Nb1.5, Nb2 and Nb2.5 in five Vickers hardness tests at the room temperature are listed in Table 2. The Nb1.5, Nb2 and Nb2.5 all exhibit excellent Vickers hardness values $> 420 \text{ HV}$. By comparing the properties of the three alloys, it can be seen that the Vickers hardness of Nb2 is the highest, which is mainly owing to the hierarchical structure without any huge primarily-precipitated phases. While the Nb1.5 is harder than Nb2.5, because the volume fraction of B2 in Nb1.5 is higher than the volume fraction of B2 in Nb2.5.

The mechanical properties of the Nb1.5, Nb2 and Nb2.5 were measured by compression tests at ambient temperature, as shown in Fig. 8. Because the samples prepared by directionally solidified technique usually has the anisotropy, the compression experiments were divided into two groups. The one is that the angle of the load direction in the compression experiment and the growth direction in directional solidifications is approximately to be 0° in Fig. 8(a), and the other one is 90° in Fig. 8(b). Therefore, the corresponding compression samples are

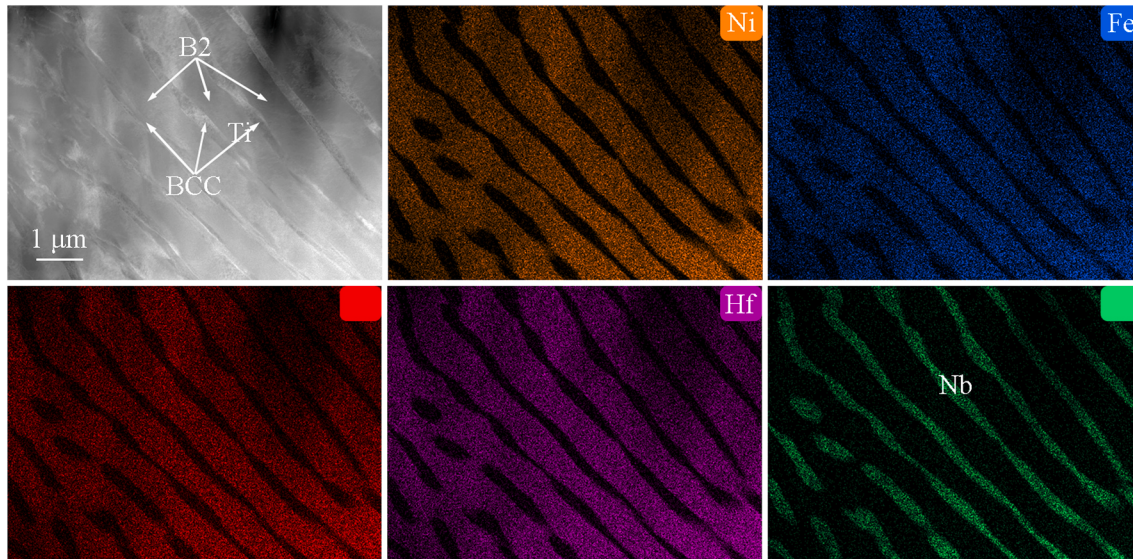


Fig. 5. The scanning transmission electron microscopy high-angle annular dark-field (STEM-HAADF) image and STEM energy dispersive spectroscopy (STEM-EDS) mappings of Ni, Fe, Ti, Hf and Nb in the Nb2 HEA.

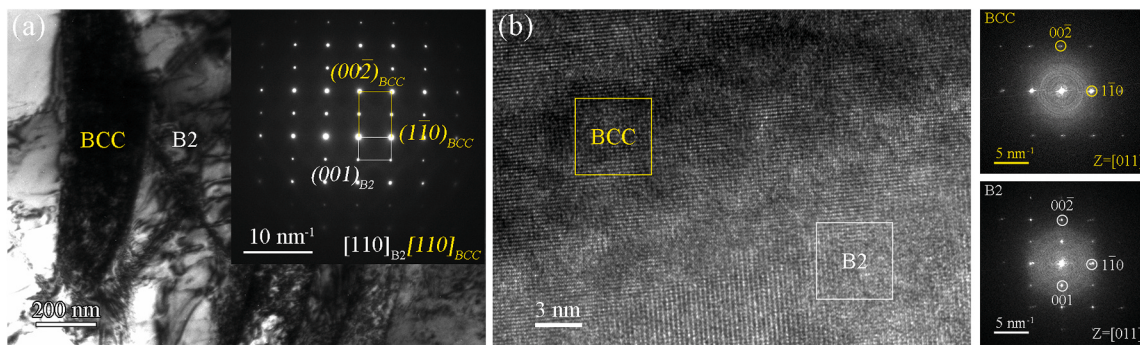


Fig. 6. (a) The TEM bright-field images parallel to [011] zone of the BCC/B2 phases. The inset shows the phase compositions of the Nb2 HE-HEA. (b) Representative high-resolution TEM image confirming the interfacial coherency with the FFTs corresponding to the BCC and B2 phases.

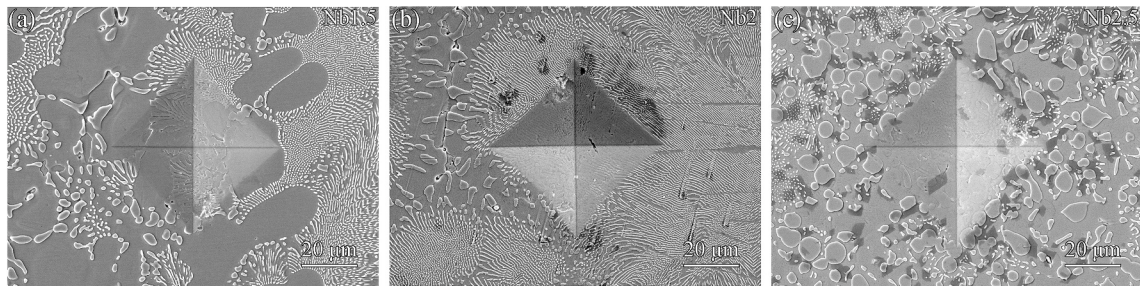


Fig. 7. The scanning electron microscope (SEM) images of the representative Vickers hardness points of (a) Nb1.5, (b) Nb2 and (c) Nb2.5.

Table 2

The average lengths of diagonal X and Y, depth, Vickers hardnesses and corresponding standard deviation values of Nb1.5, Nb2 and Nb2.5 in five Vickers hardness tests at room temperature.

	The length of diagonal X (μm)	The length of diagonal Y (μm)	Depth (μm)	Vickers hardness (HV)
Nb1.5	64.0 ± 2.2	58.7 ± 1.3	8.73 ± 0.17	496 ± 22
Nb2	61.1 ± 1.7	59.9 ± 2.1	8.62 ± 0.21	517 ± 31
Nb2.5	67.3 ± 2.5	65.2 ± 2.4	9.44 ± 0.16	425 ± 15

named as Nb1.5-0°, Nb1.5-90°, Nb2-0°, Nb2-90°, Nb2.5-0° and Nb2.5-90°, respectively. The average fracture strain, yield strength (σ_y), and corresponding standard deviations were all listed in Table 3. The Nb2-0° and Nb2-90° has the higher yield strength than the Nb1.5-0°, Nb1.5-90°, Nb2.5-0°, Nb2.5-90°. It is also worth noting that the elastic strain of Nb2-0° is approximately 3.0% in Fig. 8(a), which shows superelastic behavior. The resulting strength-ductility combination in the Nb2-0° outperforms any other compression properties of eutectic and near-eutectic HEAs in Fig. 8(c) [19–23], showing that the Nb2 alloy possesses an excellent combination of large ductility and high strength.

3.3. Deformation mechanisms

To interpret the deformation mechanism, the fracture morphologies of compression samples with different Nb concentrations were firstly observed, as shown in Fig. 9(a–c). The fracture morphology of Nb1.5-0° exhibited cleavage planes and facets, as shown in Fig. 9(a), displaying that the cleavage fracture occurred in the corresponding samples. Fig. 9(b) and (c) revealed the fracture morphology for the Nb2-0° and Nb2.5-0° samples, respectively, mainly consisting of dimple patterns. It was implied that the ductile fracture mode occurred to these alloys. These observations were consistent with the stress-strain curves in Fig. 9(a).

Secondly, the deformation microstructure with different strains was studied with TEM observations for the Nb2-0° alloy. The corresponding results are shown in Fig. 10. At the strain of ~3% in stage I, there are no apparent dislocations in BCC or B2 phases (Fig. 10(a)), showing that BCC and B2 phases are still in the elastic deformation stage instead of the plastic deformation stage. Elastic strains of B2 and BCC phases both surpassed 3%. Then, when the strain reached ~5% in stage II, it could be seen that several apparent dislocations were distributed in the BCC phase, while there were no dislocations in the B2 phase, as shown in Fig. 10(b). This phenomenon revealed that the B2 phase was still in the elastic stage, while the BCC phase yielded and started plastic deformation, which illustrated the yield strain of the B2 phase surpasses 5%, but the yield strain of the BCC phase is under 5%. Eventually, after specimen fracturing at the strain of ~22% in stage III, the deformations of the B2 and BCC phases were dominated by the slip of dislocations in the end, as shown in Fig. 10(c). Above, the evolution of deformation substructures at different strains was drawn as the schematic in Fig. 10(d).

4. Discussion

Firstly, we, by the partial similar substitution method, successfully prepared the new hierarchical eutectic Ni₃FeTi₃HfNb₂ high entropy alloys, which had the excellent mechanical property. Therefore, it proved that this method is feasible to design new hierarchical eutectic high entropy alloys.

In addition, microstructure observation and mechanical tests show that the volume fraction of the BCC phase and the resulting mechanical properties can be tailored by adjusting the Nb concentration in Fig. 11. The fracture strain and yield strength of 0° samples is all higher than those of 90° samples in Fig. 11(b) and (c). This result is similar to Ni-based superalloy [24–26]. Directionally solidified columnar crystalline materials are polycrystalline materials with <001> preferred orientation. However, with the increase of the angle, the average orientation of the columnar grains will be more and more deviated from <001>, and it is likely that they will deviate from [001] gradually along or near the [001]-[111] boundary [24–26]. Another factor affecting the fracture

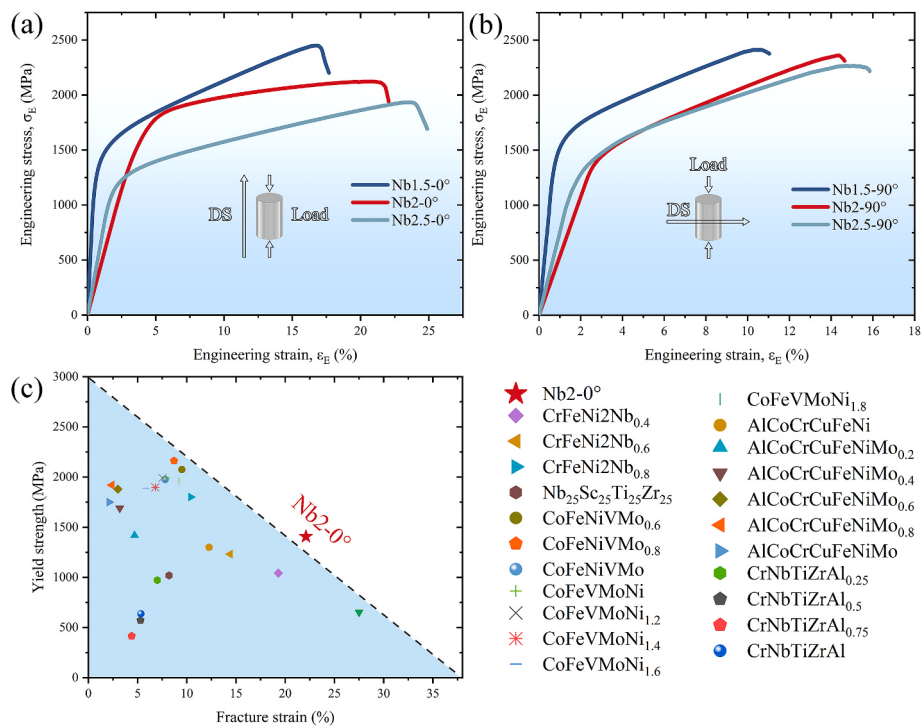


Fig. 8. (a) Representative compressive engineering stress-strain curves of the Nb1.5-0°, Nb2-0° and Nb2.5-0° at room temperature. (b) Representative compressive engineering stress-strain curves of the Nb1.5-90°, Nb2-90° and Nb2.5-90° at room temperature. (c) Yield strength-fracture strain comparison map of the compressive properties with other eutectic and near-eutectic HEAs [19–23].

Table 3

The average elastic modulus, fracture strain, yield strength and corresponding standard deviation values of Nb1.5-0°, Nb1.5-90°, Nb2-0°, Nb2-90° and Nb2.5-0° and Nb2.5-90° in five compression tests.

	Fracture strain (%)	Yield strength (MPa)
Nb1.5-0°	17.7 ± 1.2	1298 ± 40
Nb1.5-90°	10.7 ± 0.9	1264 ± 31
Nb2-0°	22.1 ± 1.9	1407 ± 36
Nb2-90°	14.6 ± 1.1	1369 ± 43
Nb2.5-0°	24.9 ± 1.6	1106 ± 49
Nb2.5-90°	15.6 ± 1.5	1052 ± 42

strain and yield strength is the grain boundary. With the increase of the angle, the grain boundary perpendicular to the stress axis increases, until all the grain boundaries are perpendicular to the stress axis at 90°. Thus, from the perspective of the influence of grain boundary, the fracture strain and yield strength has been decreasing with the increase of declination angle [24–26].

To analyze the microstructure evolution, a plot of the volume fraction of the BCC phase against the Nb concentration is shown in Fig. 11(a). Within a Nb concentration range of 15.8–23.8 at.%, the volume

fraction of the BCC phase clearly increased. The linear fitting showed that the volume fraction of the BCC phase increased by approximately 0.8% for each 1 at. % increase in the Nb concentration. Because the BCC phase mainly composed of the Nb element is softer and more plastic than the B2 phase, the fracture strain in 0° and 90° increases with an increase in the Nb concentration, as shown in Fig. 11(b). However, the yield strength and Vickers hardness do not exhibit the linear relation to the Nb concentration in Fig. 11(c) and (d). The Nb2 alloy displays the highest yield strength and Vickers hardness which is attributed to the hierarchical eutectic structure [11,16]. As shown by the hierarchical AlCoCrFeNi_{2.1} EHEA showed the yield strength of 1400 MPa, which is higher than that of non-hierarchical one without elongation sacrifice [11,16].

After comprehensively discussing anisotropy and the relationship between Nb concentration and mechanical properties, we should discuss why hierarchical eutectic structure enhanced mechanical properties in the Nb2. During the compression test, after the elastic stage in hard B2 and soft BCC phases, the soft BCC lamellae were more prone to plastic deformation. However, due to the restriction by the B2 phases in FLZ (Fig. 4(b) and (e)), which were still in the elastic stage, the soft BCC lamellae rarely proceed with plastic deformation freely. Owing to

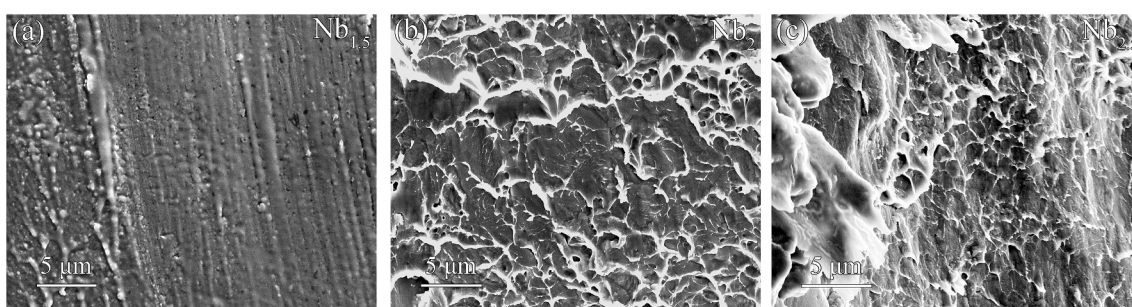


Fig. 9. The SEM images of fracture surface of (a) Nb1.5-0°, (b) Nb2-0° and (c) Nb2.5-0°.

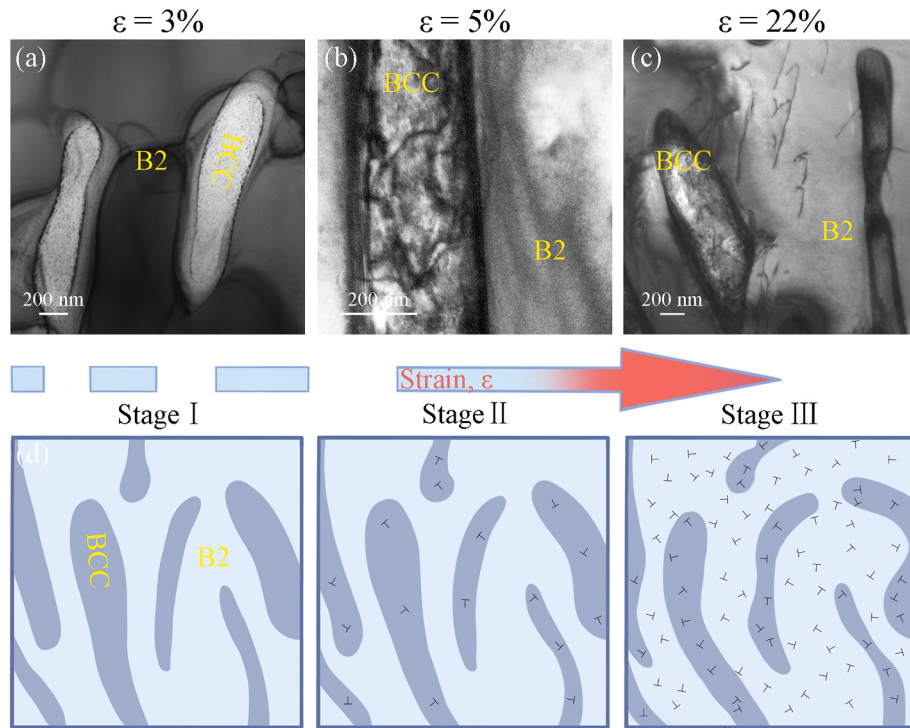


Fig. 10. The TEM bright-field images of the deformation micro-mechanism in the Nb₂-0° with different compression strain. (a) $\varepsilon = 3\%$, (b) $\varepsilon = 5\%$, (c) $\varepsilon = 22\%$. (d) the schematic of deformation micro-mechanism of the Nb₂-0°.

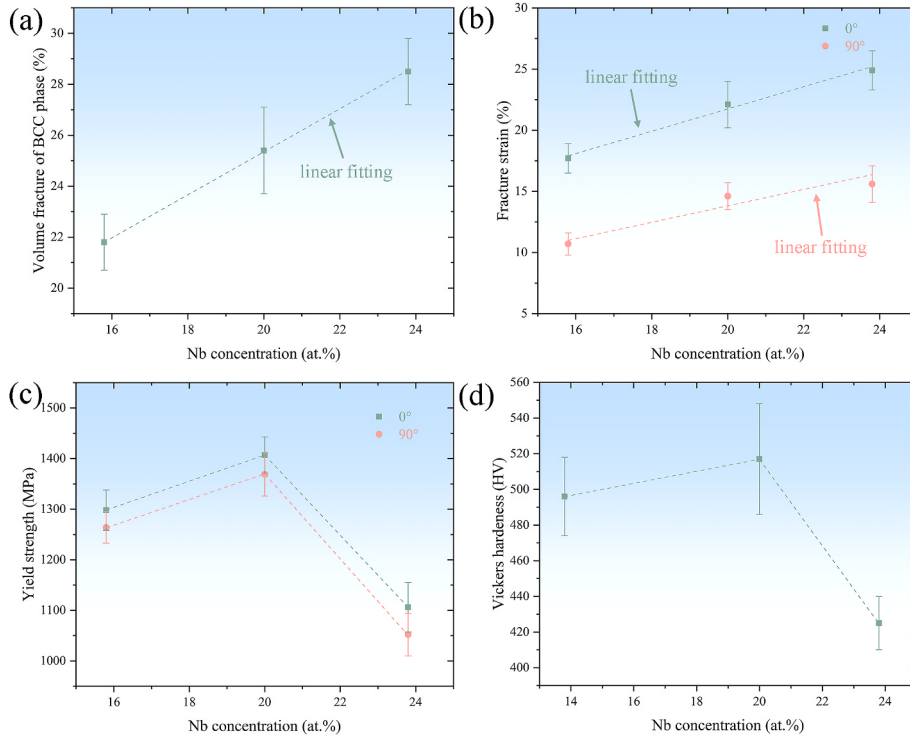


Fig. 11. Plots of (a) the volume fraction of BCC phase against the Nb concentration, (b) the fracture strain on 0° and 90° against the Nb concentration, (c) the yield strength on 0° and 90° against the Nb concentration, and (d) the Vickers hardness on against the Nb concentration.”

continuous strain, plastic-strain gradients will appear in the soft BCC lamellae [27,28]. The space of such strain gradients requires the store of geometrically necessary dislocations (GNDs). Therefore, the procedure causes a long-range back-stress, resulting in dislocations hard to transfer in BCC lamellae up to B2 phases begin to deform plastically [29]. Above

are the heterogeneous deformation effects of first-stage constraints, the heterogeneous deformation effects of second-stage constraints origins from CNZ and FNZ. The size of phase in FNZ is smaller than CNZ, so the FNZ strength is higher than CNZ. After the elastic stage, the soft CNZ is easier to plastically deform. Nevertheless, the soft CNZ are surrounded

by the hard FLZ, resulting that the CNZ cannot deform freely. Thus, this process also results in a long-range back-stress. All in all, the hierarchical eutectic structure can enhance mechanical properties due to the heterogeneous deformation effects with two-stage constraint. In addition to the hierarchical eutectic structure, the Nb2 has the elastic strain of about 3.0%, which exhibits the superelastic phenomenon. However, there are no martensitic phase before and after deformation in Figs. 5, 6 and 10. The origin of superelasticity in the Nb2 alloy was considered to be similar to the mechanism reported in Ref. [30], which was different from the traditional one of stress/strain-induced phase transformation [31].

Finally, our hierarchical eutectic HEAs and many other excellent HEAs with high yield strength and good ductility extended known performance boundaries and show a dramatically potential to increase energy efficiency and system performance in various fields, such as manufacturing and metallurgic industries. More significantly, this research provided precious experience to prepare high-performance HEAs.

5. Conclusions

In conclusion, we proposed the partial similar substitution method to successfully design and prepare hierarchical eutectic $\text{Ni}_3\text{FeTi}_3\text{HfNb}_2$ (Nb2) high entropy alloy, which has an excellent balance between ductility and strength. In addition, by microstructure observation and mechanical tests, we systematically discussed anisotropy and the relationships among microstructure evolution, mechanical property and Nb concentration. All of Nb1.5, Nb2 and Nb2.5 consist of B2 and BCC phases. Ni, Fe, Ti and Hf elements enrich in the BCC phase, while only the Nb element enriches in the B2 phase. With the content of the Nb element, there is a transformation from hypoeutectic microstructure in the Nb1.5 to eutectic one in the Nb2 to hypereutectic one in the Nb2.5. The ultrafine-grained BCC and B2 lamellar thicknesses are about ~ 200 nm and ~ 700 nm, respectively. The hierarchical eutectic structure is present in Nb2 and consists of the coarse dual-phase non-lamellar zone (CNZ) and the fine dual-phase lamellar zone (FLZ). The mechanical property of Nb2-0° outperform other eutectic and near-eutectic HEAs. Among them, Nb2-0° has the Vickers hardness of 517 HV, the high yield strength of 1407 MPa, the large fracture strain of 22.1%, and the large elastic strain of 3.0%. About anisotropy, the fracture strain and yield strength of 0° samples are higher than those of 90° samples. In addition, with the Nb concentration increasing, the volume fracture of the BCC phase and fracture strain also increase, while elastic modulus decreases. Therefore, our design method and consequences bring about a promising pathway to design high-performance hierarchical eutectic high entropy alloys.

CRediT authorship contribution statement

Huan Li: Investigation, Formal analysis, Visualization, Writing – original draft, Writing – review & editing. **Yongkang Zhou:** Writing – review & editing. **Lili Yu:** Formal analysis. **Qi Chen:** Investigation, Validation. **Weizheng Liu:** Investigation, Validation. **Shuai Zeng:** Investigation, Validation. **Huiming Zhang:** Resources, Validation. **Yuhui Zhu:** Resources, Investigation. **Hongwei Zhang:** Supervision, Resources, Writing – review & editing. **Haifeng Zhang:** Formal analysis, Supervision, Writing – review & editing. **Zhengwang Zhu:** Conceptualization, Writing – review & editing, Project administration, Funding acquisition.

Declaration of competing interest

The authors declare that they have no known competing financial interests or personal relationships that could have appeared to influence the work reported in this paper.

Data availability

Data will be made available on request.

Acknowledgments

The authors thank the financial support from the National Natural Science Foundation of China (Grant Nos. 52074257 and 51790484), the Chinese Academy of Sciences (Grant No. ZDBS-LY-JSC023).

References

- [1] J.W. Yeh, S.K. Chen, S.J. Lin, J.Y. Gan, T.S. Chin, T.T. Shun, C.H. Tsau, S.Y. Chang, Nanostructured high-entropy alloys with multiple principal elements: novel alloy design concepts and outcomes, *Adv. Eng. Mater.* 6 (2004) 299–303, <https://doi.org/10.1002/adem.200300567>.
- [2] Z.F. Lei, X.J. Liu, Y. Wu, H. Wang, S.H. Jiang, S.D. Wang, X.D. Hui, Y.D. Wu, B. Gault, P. Kontis, D. Raabe, L. Gu, Q.H. Zhang, H.W. Chen, H.T. Wang, J.B. Liu, K. An, Q.S. Zeng, T.G. Nieh, Z.P. Lu, Enhanced strength and ductility in a high-entropy alloy via ordered oxygen complexes, *Nature* 563 (2018) 546–550, <https://doi.org/10.1038/s41586-018-0685-y>.
- [3] C.Y. Lu, L.L. Niu, N.J. Chen, K. Jin, T.N. Yang, P.Y. Xiu, Y.W. Zhang, F. Gao, H. B. Bei, S. Shi, M.R. He, I.M. Robertson, W.J. Weber, L.M. Wang, Enhancing radiation tolerance by controlling defect mobility and migration pathways in multicomponent single-phase alloys, *Nat. Commun.* 7 (2016), 13564, <https://doi.org/10.1038/ncomms13564>.
- [4] W. Li, K. Xiong, L.J. Yang, S.M. Zhang, J.J. He, Y.W. Wang, Y. Mao, An ambient ductile TiHFVNbTa refractory high-entropy alloy: cold rolling, mechanical properties, lattice distortion, and first-principles prediction, *Mater. Sci. Eng., A* 856 (2022), 144046, <https://doi.org/10.1016/j.msea.2022.144046>.
- [5] S. Zeng, Y.K. Zhou, H. Li, H.W. Zhang, H.F. Zhang, Z.W. Zhu, Microstructure and mechanical properties of lightweight $\text{Ti}_3\text{Zr}_{1-x}\text{NbAl}_x$ ($x = 0, 0.25, 0.5$ and 0.75) refractory complex concentrated alloys, *J. Mater. Sci. Technol.* 130 (2022) 64–74, <https://doi.org/10.1016/j.jmst.2022.05.005>.
- [6] Q. Wei, A.J. Zhang, J.S. Han, B.B. Xin, B. Su, X.C. Wang, J.H. Meng, A novel $\text{Hf}_3\text{Nb}_{25}\text{Ta}_{25}\text{Ti}_{15}\text{Mo}_5$ refractory high entropy alloy with excellent combination of strength and ductility, *Mater. Sci. Eng., A* 857 (2022), 144035, <https://doi.org/10.1016/j.msea.2022.144035>.
- [7] Y.K. Zhou, S. Zeng, Y.H. Zhu, B.W. Zhao, H. Li, H.W. Zhang, H.F. Zhang, Z.W. Zhu, Phase decomposition and elevated temperature mechanical properties of Zr-Ti-Nb-Ta-Sn complex concentrated alloy annealed at intermediate temperatures, *Metall. Mater. Trans. A* 53 (2022) 3669–3680, <https://doi.org/10.1007/s11661-022-06774-3>.
- [8] L. Zong, L.J. Xu, C.Y. Luo, Z. Li, Y.C. Zhao, Z.N. Xu, C.H. Zhu, S.Z. Wei, Fabrication of nano-ZrO₂ strengthened WMoNbTaV refractory high-entropy alloy by spark plasma sintering, *Mater. Sci. Eng., A* 843 (2022), 143113, <https://doi.org/10.1016/j.msea.2022.143113>.
- [9] Y.P. Lu, Y. Dong, S. Duo, L. Jiang, H.J. Kang, T.M. Wang, B. Wen, Z.J. Wang, J. C. Jie, Z.Q. Cao, H.H. Ruan, T.J. Li, A promising new class of high-temperature alloys: eutectic high-entropy alloys, *Sci. Rep.* 4 (2014) 6200, <https://doi.org/10.1038/srep06200>.
- [10] J. Jin, Y. Zhou, L. Zhang, X.Y. Du, B.S. Li, A novel $\text{Fe}_{20}\text{Co}_{20}\text{Ni}_{41}\text{Al}_{19}$ eutectic high entropy alloy with excellent tensile properties, *Mater. Lett.* 216 (2018) 144–146, <https://doi.org/10.1016/j.matlet.2018.01.017>.
- [11] P.J. Shi, W.L. Ren, T.X. Zheng, Z.M. Ren, X.L. Hou, J.C. Peng, P.F. Hu, Y.F. Gao, Y. B. Zhong, P.K. Liaw, Enhanced strength-ductility synergy in ultrafine-grained eutectic high-entropy alloys by inheriting microstructural lamellae, *Nat. Commun.* 10 (2019) 489, <https://doi.org/10.1038/s41467-019-08460-2>.
- [12] P.J. Shi, R.G. Li, Y. Li, Y.B. Wen, Y.B. Zhong, W.L. Ren, Z. Shen, T.X. Zhang, J. C. Peng, X. Liang, P.F. Hu, N. Min, Y. Zhang, Y. Ren, P.K. Liaw, D. Raabe, Y. D. Wang, Hierarchical crack buffering triples ductility in eutectic herringbone high-entropy alloys, *Science* 373 (2021) 912–918, <https://doi.org/10.1126/science.abf6986>.
- [13] A. Takeuchi, A. Inoue, Classification of bulk metallic glasses by atomic size difference, heat of mixing and period of constituent elements and its application to characterization of the main alloying element, *Mater. Trans.* 46 (2005) 2817–2819, <https://doi.org/10.2320/matertrans.46.2817>.
- [14] S.J. Hao, L.S. Cui, D.Q. Jiang, X.D. Han, Y. Ren, J. Jiang, Y.N. Liu, Z.Y. Liu, S. C. Mao, Y.D. Wang, Y. Li, X.B. Ren, X.D. Ding, S. Wang, C. Yu, X.B. Shi, M.S. Du, F. Yang, Y.J. Zheng, Z. Zhang, X.D. Li, D.E. Brown, J. Li, A transforming metal nanocomposite with large elastic strain, low modulus, and high strength, *Science* 339 (2013) 1191–1194, <https://doi.org/10.1126/science.1228602>.
- [15] Y. Ma, B.B. Jiang, C.L. Li, Q. Wang, C. Dong, P.K. Liaw, F. Xu, L.X. Sun, The BCC/B2 Morphologies in $\text{Al}_x\text{NiCoFeCr}$ high-entropy alloys, *Metals* 7 (2017) 57, <https://doi.org/10.3390/met7020057>.
- [16] T. Bhattacharjee, I.S. Wani, S. Sheikh, I.T. Clark, T. Okawa, S. Guo, P. Bhattacharjee, N. Tsuji, Simultaneous strength-ductility enhancement of a nanolamellar $\text{AlCoCrFeNi}_{2.1}$ eutectic high entropy alloy by cryo-rolling and annealing 8 (2018) 3276, <https://doi.org/10.1038/s41598-018-21385-y>.
- [17] J.H. Sun, D.M. Lee, C.H. Lee, J.W. Hong, S.Y. Shin, A novel Zr-Ti-Ni-Cu eutectic system with low melting temperature for the brazing of titanium alloys near 800°C, *J. Mater. Res.* 25 (2010) 296–302, <https://doi.org/10.1557/JMR.2010.0047>.

- [18] S.J. Pennycook, Z-contrast stem for materials science, Ultramicroscopy 30 (1989) 58–69, [https://doi.org/10.1016/0304-3991\(89\)90173-3](https://doi.org/10.1016/0304-3991(89)90173-3).
- [19] W.H. Lee, Y. Oh, M.G. Jo, H.N. Han, Y. Kim, Microstructure and mechanical properties of CrFeNi₂Nb_x eutectic multicomponent alloys, J. Alloys Compd. 860 (2021), 158502, <https://doi.org/10.1016/j.jallcom.2020.158502>.
- [20] L. Rogal, J. Morgiel, Z. Swiatek, F. Czerwinski, Microstructure and mechanical properties of the new Nb25Sc25Ti25Zr25, Mater. Sci. Eng., A 651 (2016) 590–597, <https://doi.org/10.1016/j.msea.2015.10.071>.
- [21] L. Jiang, Z.Q. Cao, J.C. Jie, J.J. Zhang, Y.P. Lu, T.M. Wang, T.J. Li, Effect of Mo and Ni elements on microstructure evolution and mechanical properties of the CoFeNi_xVMo_y high entropy alloys, J. Alloys Compd. 649 (2015) 585–590, <https://doi.org/10.1016/j.jallcom.2015.07.185>.
- [22] J.M. Zhu, H.F. Zhang, H.M. Fu, A.M. Wang, H. Li, Z.Q. Hu, Microstructures and compressive properties of multicomponent AlCoCrCuFeNiMo_x alloys, J. Alloys Compd. 497 (2010) 52–56, <https://doi.org/10.1016/j.jallcom.2010.03.074>.
- [23] M. Zhu, L.J. Yao, Y.Q. Liu, M. Zhang, K. Li, Z.Y. Jian, Microstructure evolution and mechanical properties of a novel CrNbTiZrAl_x ($0.25 \leq x \leq 1.25$), Mater. Lett. 272 (2020), 127869, <https://doi.org/10.1016/j.matlet.2020.127869>.
- [24] J. Zhang, Z.Q. Jie, T.W. Huang, W.C. Yang, L. Liu, H.Z. Fu, Research and development of equiaxed grain solidification and forming technology for Nickel-based cast superalloys, Acta Metall. Sin. 55 (2019) 1145–1159, <https://doi.org/10.11900/0412.1961.2019.00088>.
- [25] Q.Y. Xu, C. Yang, X.W. Yan, B.C. Liu, Development of numerical simulation in Nickel-based superalloy turbine blade directional solidification, Acta Metall. Sin. 55 (2019) 1175–1184, <https://doi.org/10.11900/0412.1961.2019.00126>.
- [26] J. Zhang, L. Wang, D. Wang, G. Xie, Y.Z. Lu, J. Shen, L.H. Lou, Recent progress in research and development of Nickel-based single crystal superalloys, Acta Metall. Sin. 55 (2019) 1077–1094, <https://doi.org/10.11900/0412.1961.2019.00122>.
- [27] K. Lu, Making strong nanomaterials ductile with gradients, Science 345 (2014) 1455–1456, <https://doi.org/10.1126/science.1255940>.
- [28] X.L. Wu, M.X. Yang, F.P. Yuan, G.L. Wu, Y.J. Wei, X.X. Huang, Y.T. Zhu, Heterogeneous lamella structure unites ultrafine-grain strength with coarse-grain ductility, Proc. Natl. Acad. Sci. U.S.A. 112 (2015) 14501–14505, <https://doi.org/10.1073/pnas.1517193112>.
- [29] E. Ma, T. Zhu, Towards strength-ductility synergy through the design of heterogeneous nanostructures in metals, Mater. Today 20 (2017) 323–331, <https://doi.org/10.1016/j.mattod.2017.02.003>.
- [30] H.Y. Chen, Y.D. Wang, Z.H. Nie, R.G. Li, D.Y. Cong, W.J. Liu, F. Ye, Y.Z. Liu, P. Y. Cao, F.Y. Tian, X. Shen, R.C. Yu, L. Vitos, M.H. Zhang, S.L. Li, X.Y. Zhang, H. Zheng, J.F. Mitchell, Y. Ren, Unprecedented non-hysteretic superelasticity of [001]-oriented NiCoFeGa single crystals, Nat. Mater. 19 (2020) 712–718, <https://doi.org/10.1038/s41563-020-0645-4>.
- [31] Y.J. Shi, S.L. Li, T.L. Lee, X.D. Hui, Z.W. Zhang, R.G. Li, M.H. Zhang, S. Kabra, Y. D. Wang, In situ neutron diffraction study of a new type of stress-induced confined martensitic transformation in Fe₂₂Co₂₀Ni₁₉Cr₂₀Mn₁₂Al₇ high-entropy alloy, Mater. Sci. Eng., A 771 (2020), 138555, <https://doi.org/10.1016/j.msea.2019.138555>.